Research Square

Preprints are preliminary reports that have not undergone peer review.
They should not be considered conclusive, used to inform clinical practice,
or referenced by the media as validated information.

Cation Diffusion in $ZnAl_2O_4$, Zn_2SiO_4, and Their Heterogeneous Interface: A Machine- Learning Molecular Dynamics Study

Kaixin Zhang
Southwest University of Science and Technology
Peng Bi
Southwest University of Science and Technology
Yong Yi
Southwest University of Science and Technology
Enzhu Li
University of Electronic Science and Technology of China
Xu Huang
Southwest University of Science and Technology
Jingsong Liu
feram@163.com

Southwest University of Science and Technology

Research Article

Keywords: $ZnAl_2O_4$, Zn_2SiO_4, Heterogeneous interface, Molecular Dynamics Simulation, Diffusion

Posted Date: November 24th, 2026

DOI: https://doi.org/10.21203/rs.3.rs-11750996/v1

License: This work is licensed under a Creative Commons Attribution 4.0 International License.
Read Full License

Additional Declarations: No competing interests reported.

Cation Diffusion in $ZnAl_2O_4$, Zn_2SiO_4, and Their Heterogeneous Interface: A Machine-Learning Molecular Dynamics Study

Kaixin Zhang[a], Peng Bi[b], Yong Yi[a], Enzhu Li[c] , Xu Huang[a*], Jingsong Liu[a*],

[a] *School of Materials and Chemistry, Southwest University of Science and Technology, Mianyang 621010, China*

[b] *School of Mathematics and Physics, Southwest University of Science and Technology, Mianyang 621010, China*

[c] *National Engineering Research Center of Electromagnetic Radiation Control Materials, University of Electronic Science and Technology of China, Chengdu, 610054, China*

Abstract:

Filters have been applied extensively in many areas including radar, mobile communications and satellite communications; progress in integration has also been closely related with Low-Temperature Co-fired Ceramic (LTCC), Low-Temperature Co-fired Ferrite (LTCF). During the co-firing process of ceramics and ferrite, the atomic movement and cation diffusion near the interface are complex phenomena, and the microscopic mechanisms behind them urgently require further study. In this study, machine-learning molecular dynamics (MLMD) simulations were employed to investigate atomic motion and cation diffusion in $ZnAl_2O_4$, Zn_2SiO_4, and their heterogeneous interface. It was observed that the diffusion activation energy varies depending on the cation in the doped solid phase. The diffusion activation energies of B^{3+}, Si^{4+} and Ti^{4+} doped in $ZnAl_2O_4$ are 0.315 eV, 0.607 eV and 0.417 eV, respectively. The diffusion activation energies of Al^{3+}, B^{3+} and Ti^{4+} doped in Zn_2SiO_4 are 0.240 eV, 0.147 eV and 0.172 eV, respectively. There are obvious differences in the diffusion behavior of different cations at the heterogeneous interface. The order of migration ability along the normal direction of the interface is $Zn^{2+} > Si^{4+} > Al^{3+}$.This work provides an atomic-scale reference for interface diffusion analysis and co-firing process of ceramic-ferrite components by analyzing the cation migration rules of $ZnAl_2O_4$, Zn_2SiO_4 and their heterogeneous interfaces.

Key words: $ZnAl_2O_4$, Zn_2SiO_4, Heterogeneous interface, Molecular Dynamics Simulation, Diffusion

[*] *Corresponding author. E-mail address: xuhuangswust@foxmail.com (X. Huang)*

Corresponding author. E-mail address: feram@163.com (J. Liu)

1. Introduction

Filters are critical frequency-selective components in radar, satellite, and mobile communication systems, and their insertion loss and operational stability significantly affect overall system performance[1, 2]. With the rapid development of high-frequency technologies, including 5G/6G communications, in-vehicle networks, and wearable electronic devices, filters must operate at higher frequencies, requiring smaller sizes, lighter, higher integration, and lower losses[3, 4]. To meet these goals, material systems and integration processes that combine high-frequency performance with reliable device fabrication capabilities have been continuously developed[5, 6]. Because filters must meet comprehensive requirements for dielectric, magnetic, and structural integration; ceramics and ferrites are usually integrated together within one device by layered co-firing[7, 8]. This multilayer stacked structure enables passive components to be miniaturized, lightweight, and has high-reliability integration capabilities[9]. The two materials must form a strong interface during co-firing, while retaining as much as possible of their original dielectric and magnetic properties[10].

There are significant differences in the crystal structure between ceramics and ferrites. This makes them face many problems in the co-firing process, including mismatch of coefficient of thermal expansion, inconsistent sintering shrinkage rate, interface reaction and cation diffusion. It is easy to cause delamination, deformation and cracking of the co-fired interface, and also lead to the decrease of interface bond strength and the degradation of electromagnetic properties[11]. During the co-sintering of heterogeneous composite materials, cation diffusion is an inevitable microscopic phenomenon. Moderate interfacial cation diffusion helps to form a stable interfacial transition layer, which is usually thin and dense, and can alleviate thermal stress and shrinkage mismatch. The interfacial bonding strength and mechanical stability are improved, and the co-sintering process is more stable[12, 13]. Therefore, uncovering how ions migrate across the interface is crucial to understanding what occurs during ceramic-ferrite co-firing.

LTCC technology enables the combination of dielectric ceramics, conductive electrodes, and other functional materials into multilayer electronic components. Glass-ceramic composites of LTCC materials can crystallize to $ZnAl_2O_4$ and Zn_2SiO_4. The reaction between ZBS glass ($ZnO–B_2O_3–SiO_2$) and Al_2O_3 during the sintering process leads to the formation of $ZnAl_2O_4$ and Zn_2SiO_4 as the most prevalent crystalline phases. The relative contents of these phases depend on the composition and sintering temperature, influencing the microstructure and dielectric properties of the composites[14]. These findings underscore the relevance of $ZnAl_2O_4$ and Zn_2SiO_4 to LTCC dielectric materials and motivate further investigation of atomic transport in these oxide phases.

The ZnO/Al_2O_3 double layer, the formation of $ZnAl_2O_4$ spinel and the growth of the reaction layer have been experimentally studied. These are highly interface and grain boundary solid state diffusion processes[15]. DFT calculations have investigated intrinsic defects in $ZnAl_2O_4$[16]. First-principles calculations of ferrite have revealed

vacancy-mediated cation migration pathways and demonstrated that migration barriers depend on the local coordination environment and crystal-field effects[17]. These findings verify the importance of defect chemistry and local atomic structure to control cation transport.

Traditional experimental methods are difficult to directly reveal the high temperature diffusion behavior at the atomic scale. In contrast, MLMD based on machine learning force field can reduce the computational cost of large-scale and long-time scale atomic simulation, while maintaining the accuracy close to that of first-principles calculation[18, 19]. Studies have shown that MLMD method can be used to investigate cation transport, molecular transport, heterogeneous interfaces and diffusion dynamics in solid electrolytes[20-23]. The MLMD method has previously been used to resolve the cation transport in NiCuZn ferrite and at its homogeneous interfaces[24]. Unlike the homogeneous interfaces reported therein, the present model integrates two different crystal structures. It enables investigation of how variations in local coordination and interfacial atomic arrangement modulate cation mobility. The resulting contrast provides an atomic-level basis for understanding diffusion between different oxide phases and offers insights into interfacial transport during ceramic co-firing.

In this study, density functional theory (DFT) calculations, neuroevolutionary potential (NEP) and MLMD were employed to study the cation diffusion mechanism in $ZnAl_2O_4$, Zn_2SiO_4 doped cations and their heterogeneous interfaces. It is expected to provide a reference for future research on diffusion and interface evolution in co-fired ceramic systems.

2. Calculation Methods

2.1 Structures

$ZnAl_2O_4$ is a typical cubic spinel and is in the cubic crystal system. In its crystal structure, Zn^{2+} occupies the tetrahedral A site, Al^{3+} mainly occupies the octahedral B site, and oxygen ions form a cubic close-packed skeleton. Cations and oxygen ions in different coordination environments are connected to each other to form a crystal structure with three-dimensional periodic characteristics.

Zn_2SiO_4 is a typical willemite structure and is in the trigonal crystal system. Zn^{2+} and Si^{4+} are both in tetrahedral coordination environment in its crystal structure to form ZnO_4 and SiO_4 tetrahedrons respectively. These tetrahedrons are linked together by common oxygen atoms to make a crystal skeleton with a three-dimensional periodic structure.

The $ZnAl_2O_4$ doping model is built based on the 5×5×5 supercell. Independent single doping models are established respectively. Each time only one of B^{3+}, Si^{4+} and Ti^{4+} ions is used to replace 10% of Al^{3+}. The replacement of Al^{3+} by Si^{4+} and Ti^{4+} leaves the charge difference to be compensated by Zn vacancies. The Zn_2SiO_4 doping model is based on a 4×4×4 supercell. Al^{3+}, B^{3+}, and Ti^{4+} are used to individually replace 10% of Si^{4+} to construct independent doping systems without simultaneous doping of

multiple ions. The Al-terminated $ZnAl_2O_4(111)$ surface and the $Zn_2SiO_4(001)$ surface were chosen as the components of the interface to construct the $ZnAl_2O_4/Zn_2SiO_4$ heterogeneous interface. The corresponding surface models were constructed using a (10×10) supercell for $ZnAl_2O_4(111)$ and a (4×4) supercell for $Zn_2SiO_4(001)$. The in-plane lattice parameters of $Zn_2SiO_4(001)$ were used as the reference for evaluating the lattice mismatch, yielding a mismatch of approximately 2.49%. The two slabs were then stacked in the interface-normal direction to construct the heterogeneous interface model. A vacuum layer of 15 Å was included along the interface-normal direction.

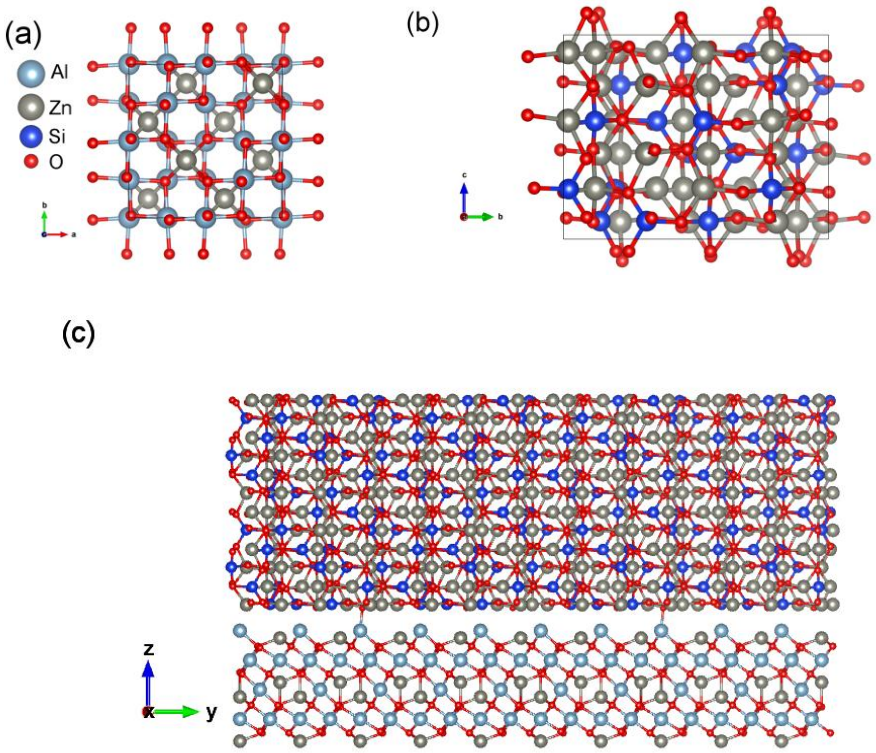

Fig. 1. Crystal structure (a) $ZnAl_2O_4$, (b) Zn_2SiO_4, (c) Heterogeneous interface

2.2 NEP Potential Function

The training dataset consists of pure and doped phases of $ZnAl_2O_4$, pure and doped phases of Zn_2SiO_4 and $ZnAl_2O_4/Zn_2SiO_4$ heterogeneous interface. Lattice perturbation, shear strain and atomic position perturbation structures were generated using NepTrainkit[25] software, a total of 2396. Density functional theory (DFT) calculations with the Perdew-Burke-Ernzerhof (PBE) exchange correlation functional were used to calculate single point energy. The cutoff energy of plane waves is consistently 500 eV and the Monkhorst-Pack grid k-point density is 0.03. When calculating the energy of a single point, the sum of the energies tends to 10 -5 eV per atom[26, 27].

In conventional DFT, the Local Density Approximation (LDA) or the Generalized Gradient Approximation (GGA) is insufficient for describing strongly correlated local 3d electrons and contains self-interaction errors. The DFT+U method corrects for Coulomb self-interactions by introducing the Hubbard U parameter on local d orbitals

(such as Ti 3d) to account for on-site electron-electron correlation effects. The Hubbard-U parameter of Ti was set to 4.0 eV[28] to correct the localized behavior of 3d electrons, thereby improving the accuracy of electronic structure calculations.

The data were randomly split into a training set and test set in an 8:2 ratio. The NEP was chosen to parameterize the interaction between atoms[29]. In the case of the angular basis functions, the three-body, four-body and five-body terms have expansion orders of 4, 2 and 1 respectively. The training was performed for a total of 2.5×10^5 steps. Fig. 2 also shows the training and testing losses over time, and the root mean square error (RMSE) of energy and force during training. The maximum RMSE for energy on the training set is 9.09 meV/atom, and the maximum RMSE for force is 216.74 meV/A; on the test set, the maximum RMSE for energy is 9.12 meV/atom, and the maximum RMSE for force is 216.53 meV/A. The error values for the training and test sets were similar, indicating no significant overfitting. The RMSE for the training and test sets are comparable, with no significant overfitting observed.

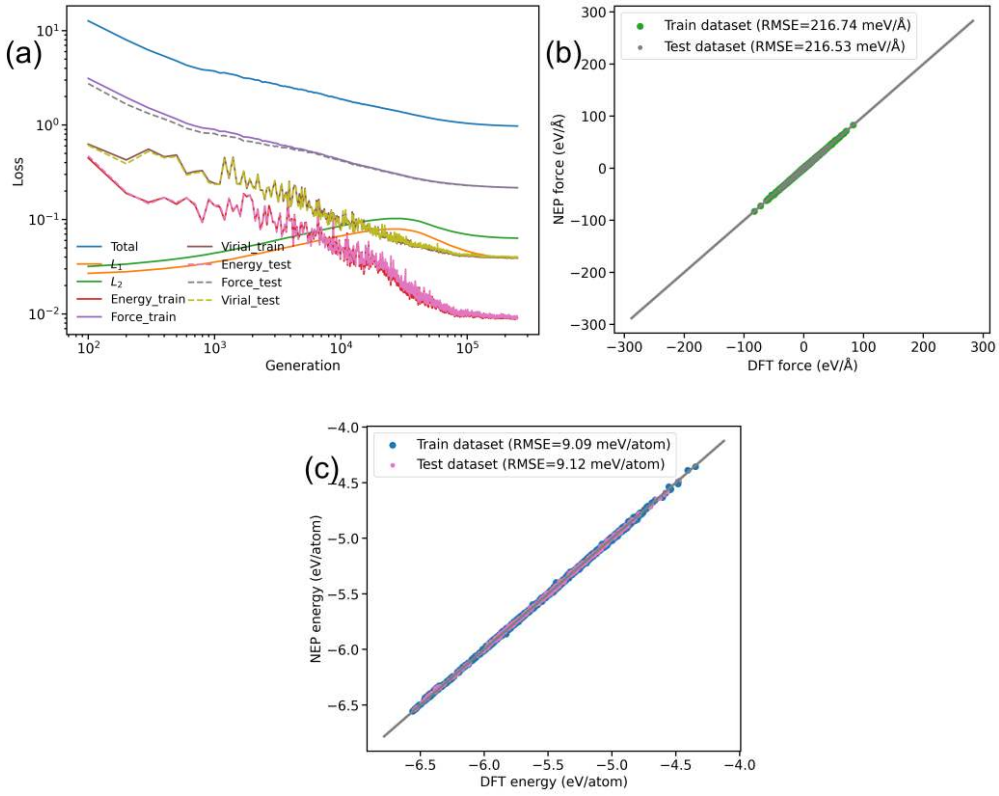

Fig. 2. (a) Loss function plot; (b) Root-mean-square force error plots for the training and test sets; and (c) Root-mean-square energy error plots for the training and test sets

2.3 Molecular Dynamics Simulation

GPUMD was used to perform molecular dynamics simulations. The simulations were conducted over a temperature range of 300–1500 K, with a time step of 1 fs and a duration of 200 ps per run. All simulations were performed under the NPT ensemble and the Berendsen coupling method was used to keep the pressure constant[30]. The

mean square displacement (MSD) of each cation species in the entire simulated temperature range was recorded from the obtained trajectory, and the corresponding diffusion coefficient was calculated accordingly. The diffusion coefficient is calculated from the mean square displacement within the diffusion interval[31]:

$$\boldsymbol{D = \frac{1}{2Nd\Delta t}\sum_{i=1}^{N}\left\langle |r_i(\tau + t) - r_i(\tau)|^2 \right\rangle_\tau} \quad (1)$$

In the formula, D is the cation diffusion coefficient; N is the number of diffusing ions participating in the statistics; d is the dimension of the simulation system, and d=3 is taken for the three-dimensional simulation; Δt is the lag time; $r_i(\tau)$、$r_i(\tau + t)$ represent the position of the i-th cation at the reference time τ and $\tau + t$ respectively; $\langle ... \rangle_\tau$ represents the time ensemble average of all starting moments τ; this formula is only applicable to the linear diffusion interval of the MSD-t curve.

The temperature dependence of the diffusion coefficients was then fitted to the Arrhenius relationship to determine the diffusion activation energies:

$$\boldsymbol{D = D_0 \exp(-\frac{E_a}{k_B T})} \quad (2)$$

In this equation, D_0 is the pre-exponential factor, E_a denotes the diffusion activation energy, k_B is the Boltzmann constant, and $k_B = 8.617\times10^{-5}$ eV·K^{-1}.

3. Results and Discussion

3.1. Potential Function Verification

The machine-learning potential was validated in terms of lattice constants and thermal expansion behavior. The changes in the lattice parameters of $ZnAl_2O_4$ and Zn_2SiO_4 at the temperature range of 300-1500 K were calculated using molecular dynamics simulations and compared to experimental data and DFT calculations found in the literature.

The lattice constants a, b and c of $ZnAl_2O_4$ increase gradually with the temperature as depicted in Fig. 3(a). The total change is about linear. The largest difference between the results obtained by calculations and the available experimental data and DFT results was 1.6%[32-36]. According to the correlation between the lattice constants and temperature, the coefficient of thermal expansion of $ZnAl_2O_4$ was determined to be about 12.6×10^{-6} K^{-1}, which is near to the experimental findings[37].

The thermal expansion of Zn_2SiO_4 has directional differences as illustrated in Fig. 3(b) and (c). With the temperature increases, the lattice constants along the a, b, and c axes gradually increase. The change in the magnitude of the c axis is different than that of the a and b axes, which means that its thermal expansion is anisotropic. The trends of the calculated lattice parameters are overall consistent with the experimental results published in literature and DFT calculations with an error less than 2 percent, which

supports the validity of the use of the potential function to the Zn_2SiO_4 crystal structure[38-41]. The thermal expansion coefficients are about $\alpha_a = \alpha_b = 7.35 \times 10^{-6}$ K^{-1} and $\alpha_c = 7.96 \times 10^{-6}$ K^{-1}, consistent with the trends observed in experiments[42].

These verification results show that the trained NEP potential function can reproduce the lattice structure of $ZnAl_2O_4$ and Zn_2SiO_4 and their thermodynamic responses as the temperature changes.

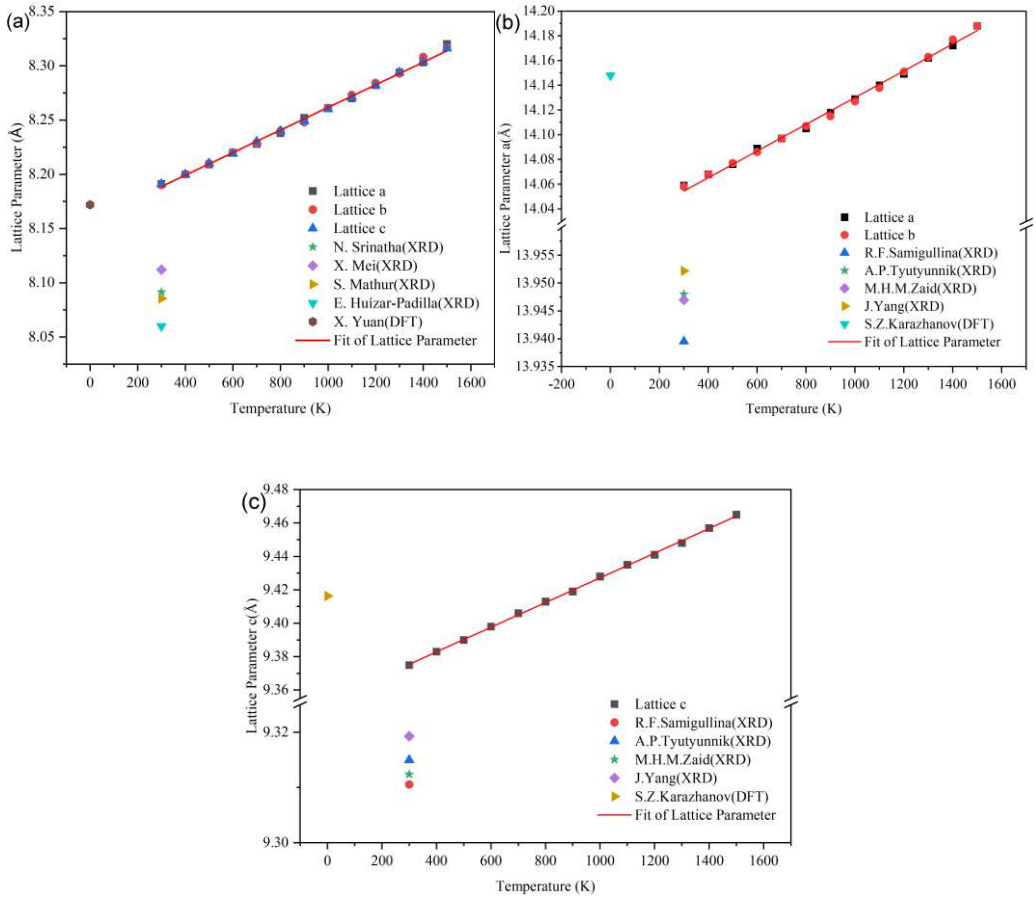

Fig. 3. (a) Temperature dependence of the lattice parameters of $ZnAl_2O_4$;(b)Temperature dependence of the a- and b-axis lattice parameters of Zn_2SiO_4;(c)Temperature dependence of the c-axis lattice parameter of Zn_2SiO_4

3.2 Diffusion of Dopant cations in the Bulk lattice

3.2.1 Fitting the Arrhenius Equation for Cation Diffusion

The diffusion coefficients of different dopant cations in the $ZnAl_2O_4$ and Zn_2SiO_4 lattices were computed at the temperature range of 600-1500 K and the data on diffusion were fitted by the Arrhenius equation. The fitting results of various ions were compared to analyze their diffusion behavior and thermal activation characteristics.

Doping of heterovalent cations creates charge compensating vacancies. In the case of $ZnAl_2O_4$, replacement of Al^{3+} with Si^{4+} and Ti^{4+} results in the creation of zinc vacancies to ensure overall charge neutrality. In Zn_2SiO_4, replacement of Si^{4+} by

$Al^{3+}$and B^{3+} results in oxygen vacancies for charge compensation. These vacancy defects provide available sites for cation migration, while the local lattice distortions induced by the dopant cations further regulate the diffusion activation energies along the diffusion paths.

Fig. 4(a) indicates that in the temperature range of 600-1500 K, the diffusion coefficients of B^{3+}, Si^{4+}, and Ti^{4+} in the $ZnAl_2O_4$ doped system tend to increase with increasing temperature. It is in line with the general law of thermally activated diffusion. The higher the temperature, the more atoms vibrate and enable more atoms to cross the migration barrier and diffuse through the crystal lattice. Based on the Arrhenius fit results, the apparent diffusion activation energies for B^{3+}, Si^{4+}, and Ti^{4+} are 0.315 eV, 0.607 eV, and 0.417 eV, respectively. The diffusion activation energy of Si^{4+} is the largest and that of B^{3+} is the smallest, which means that under the conditions of the experiment, the diffusion of Si^{4+} is more challenging than that of B^{3+}.

The variation in diffusion activation energy of various doped cations is not only connected with the ionic radius, but also influenced by the local coordination environment and metal-oxygen bonding. All B^{3+}, Si^{4+}, and Ti^{4+} substitute the octahedral Al^{3+} sites in $ZnAl_2O_4$ and their ionic radii are about 0.27 Å, 0.40 Å and 0.605 Å, respectively. A smaller ion radius may be beneficial to reducing geometric constraints during migration, but ion size does not alone determine the level of diffusion activation energy. The ionic radius of Si^{4+} is smaller than that of Ti^{4+}, but its diffusion activation energy is higher, indicating that local structure and chemical bonding may also have an important impact on the migration behavior of cations. This phenomenon may be because the interaction between different doped cations and the surrounding O^{2-} may affect the reconstruction of the local structure during the migration process, and the bonding strength of the Ti-O bond is weaker than that of the Si-O bond.

The diffusion coefficients of Al^{3+}, B^{3+} and Ti^{4+} in the doped Zn_2SiO_4 system are to be lager as indicated in Fig. 4(b) with increasing temperature. The apparent diffusion activation energies of Al^{3+}, B^{3+} and Ti^{4+} are 0.240 eV, 0.147 eV and 0.172 eV respectively. Among these cations, Al^{3+} has the largest diffusion activation energy, while B^{3+} has the smallest.

The diffusion behavior in Zn_2SiO_4 may not be fully explained by ionic radius alone. Other factors such as local coordination environment, lattice relaxation, and defect chemistry also affect cation migration. In the model used in this article, when Al^{3+} or B^{3+} replaces Si^{4+}, it will be accompanied by the generation of oxygen vacancies to achieve charge compensation; while the substitution of Ti^{4+} is an equivalent substitution and does not require additional charge compensation. Therefore, the experimentally observed difference in diffusion activation energy may be the result of a combination of cation size, local structural rearrangement, and defect chemistry. The Arrhenius equation obtained by fitting the diffusion coefficient of doped cations is summarized in Table 1.

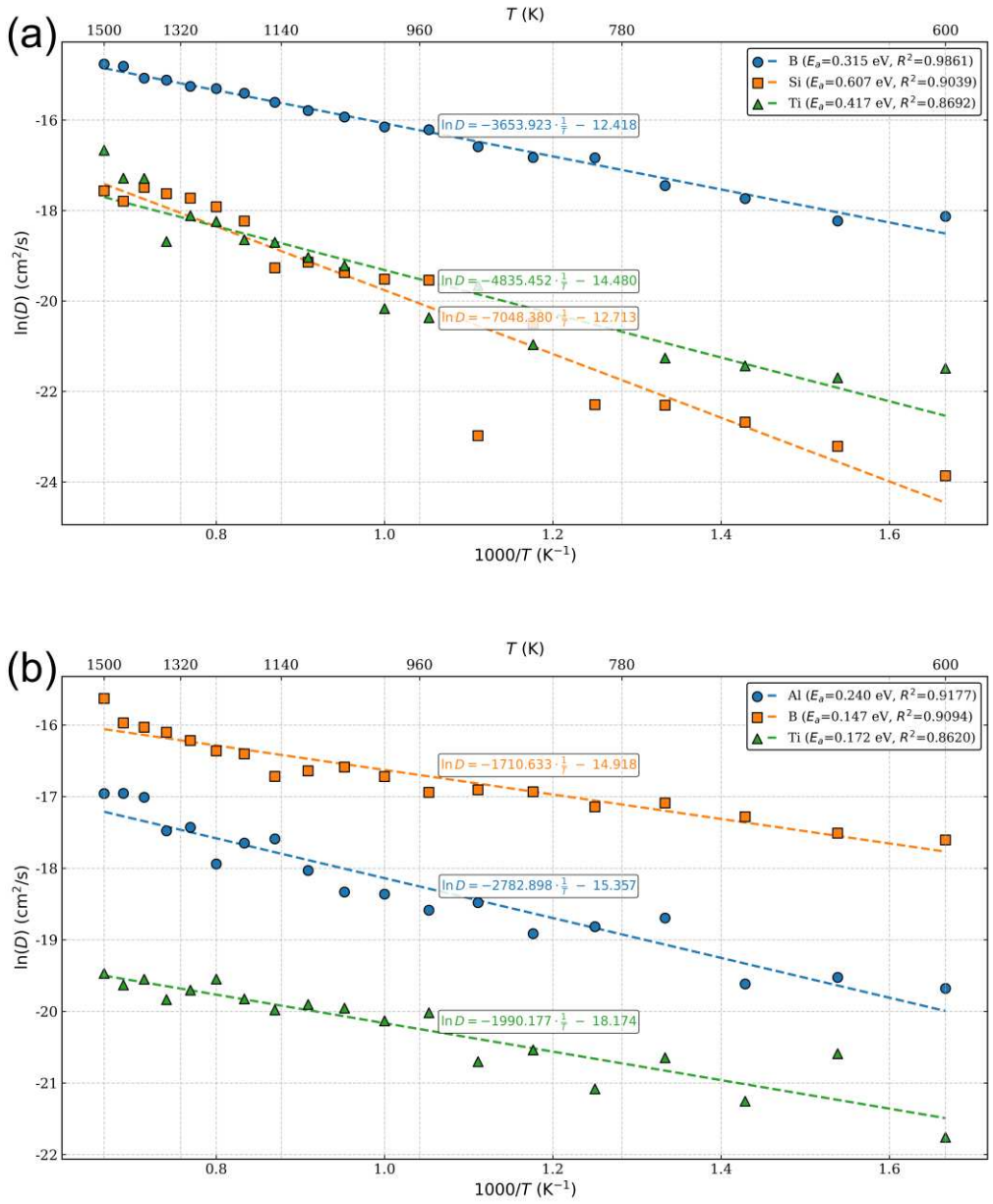

Fig. 4. Arrhenius plots for the diffusion (a) $ZnAl_2O_4$ dopants and (b) Zn_2SiO_4 dopants

Table 1

The Arrhenius Expression for Cation Diffusion

Crystal structures	Cation	R^2	Arrhenius Expression (cm^2/s)
$ZnAl_2O_4$	B^{3+}	0.9861	$\boldsymbol{D = 4.045 \times 10^{-6} exp\left(-\frac{0.315}{k_B T}\right)}$
	Si^{4+}	0.9039	$\boldsymbol{D = 3.012 \times 10^{-6} exp\left(-\frac{0.607}{k_B T}\right)}$

	Ti^{4+}	0.8692	$\boldsymbol{D = 5.145 \times 10^{-7} exp\left(-\frac{0.417}{k_B T}\right)}$
	Al^{3+}	0.9177	$\boldsymbol{D = 2.141 \times 10^{-7} exp\left(-\frac{0.240}{k_B T}\right)}$
Zn_2SiO_4	B^{3+}	0.9094	$\boldsymbol{D = 3.320 \times 10^{-7} exp\left(-\frac{0.147}{k_B T}\right)}$
	Ti^{4+}	0.8620	$\boldsymbol{D = 1.280 \times 10^{-8} exp\left(-\frac{0.172}{k_B T}\right)}$

3.2.2 Temperature Dependence of the Diffusion Coefficient of Doped Cations

To compare the diffusion behavior of different dopant cations in the $ZnAl_2O_4$ and Zn_2SiO_4 lattices, the diffusion coefficients of each dopant element were calculated over the temperature range of 600–1500 K, as shown in Fig. 5. The diffusion coefficients of the dopant elements in both lattices increase with rising temperature, indicating that higher temperatures enhance atomic thermal motion and promote atomic migration. This behavior is consistent with the expected temperature dependence of a thermally activated migration process.

There are two quantities that jointly determine the size of the diffusion coefficient: diffusion activation energy and pre-exponential factor. Among them, diffusion activation energy reflects the energy barrier that needs to be overcome during cation migration, while the pre-exponential factor is closely related to factors such as the frequency of migration attempts and the local atomic structure environment. Therefore, the diffusion coefficients of different doped cations are not only determined by the diffusion activation energy, but are the result of the combined effect of the two.

In the $ZnAl_2O_4$ doped system, as shown in Fig. 5(a), B^{3+} exhibits the highest diffusion coefficient in the $ZnAl_2O_4$ lattice in the studied temperature range. At relatively low temperatures (600–1000 K), Ti^{4+} is more diffusible than Si^{4+}. As the temperature increases, the difference in diffusion coefficient between the two becomes smaller, and both curves show obvious fluctuations.

In the doped Zn_2SiO_4 system, as shown in Fig. 5(b), B^{3+} always shows the highest diffusion coefficient, followed by Al^{3+} and Ti^{4+}. This order remains unchanged over the temperature range studied. The activation energies of B^{3+} and Ti^{4+} are close, but B^{3+} shows a significantly higher diffusion coefficient. This difference is related to the larger exponential factor of B^{3+}, which enhances its overall diffusivity. Furthermore, the relatively high diffusion activation energy of Al^{3+} does not prevent it from exhibiting higher diffusivity than Ti^{4+}, demonstrating the important contribution of the exponential factor to the overall diffusion behavior.

In the two systems of $ZnAl_2O_4$ and Zn_2SiO_4 , the diffusion coefficient of B^{3+} is the highest, indicating that B^{3+} has relatively strong migration ability in these two crystal structures. However, the relative diffusion behavior of the remaining cations is different in the two systems. In $ZnAl_2O_4$, the relative diffusion coefficients of Ti^{4+} and Si^{4+} change with temperature; while in Zn_2SiO_4, the diffusion coefficients of each ion always satisfy the order of $B^{3+} > Al^{3+} > Ti^{4+}$. The above differences indicate that the cation diffusion process is not only controlled by the migration activation energy, but also related to pre-exponential factors and the local atomic environment. The completely different crystal structures and charge compensation defect configurations of the two host materials will further cause differences in cation migration behavior.

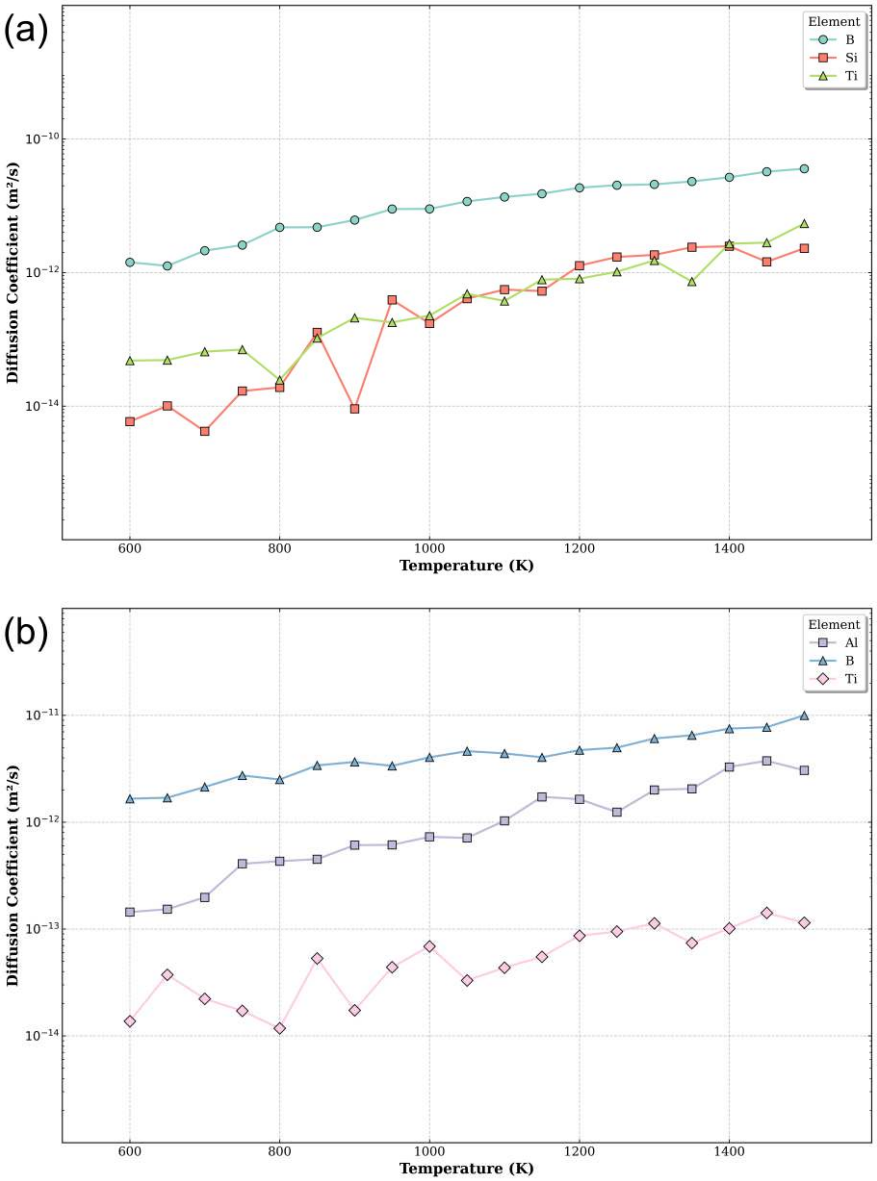

Fig. 5. Variation of diffusion coefficients of various cations with temperature

(a) $ZnAl_2O_4$ dopants (b) Zn_2SiO_4 dopants

3.3 Cation Diffusion at Heterogeneous Interfaces

To investigate atomic diffusion behavior in $ZnAl_2O_4/Zn_2SiO_4$ heterostructures, this study further developed a model of the pure $ZnAl_2O_4/Zn_2SiO_4$ heterogeneous interface. This interface was constructed by stacking $ZnAl_2O_4(111)$ and $Zn_2SiO_4(001)$ crystal planes along the normal to the interface after matching their crystal planes.

The heterogeneous interface is constructed by the matching combination of ZnAl2O4(111) crystal face and Zn2SiO4(001) crystal face. The ZnAl2O4(111) plane has three surface cut-off configurations Zn atom end, Al atom end, and O atom end cut-off plane, which are coupled with the Zn2SiO4(001) surface respectively. The slab consists of one unit-cell layer of $Zn_2SiO_4(001)$ and two unit-cell layers of $ZnAl_2O_4(111)$. This model takes into account both computational cost and efficiency while retaining key interface features. All heterogeneous interface models are uniformly fixed to 224 atoms to avoid errors in energy comparison caused by different termination configurations due to unequal total number of atoms.

In order to select the most stable interface model and determine the optimal interface spacing of the interface model, consider using the interface adhesion work (W_{ad}) to determine:

$$\boldsymbol{W_{ad} = \frac{E_x + E_y - E_{xy}}{A}} \tag{3}$$

E_x and E_y are the total energy of surface *x* and surface *y* after structural optimization respectively; E_{xy} represents the total energy of the interface model; A represents the surface area of the interface.

W_{ad} is a basic physical quantity of the interface model, and its definition is the energy required to reversibly separate the interface into two free surfaces. The binding force of atoms between interfaces is positively correlated with W_{ad}. Therefore, the stability of the interface can be judged by W_{ad}. Fig. 6 shows the variation curve of W_{ad} with interface spacing for three groups of interface models. Table 2 is compiled, which lists the specific values of W_{ad} corresponding to the three interface models under their respective optimal interface spacing. The $ZnAl_2O_4(111)$ cutoff surface was selected as Al atom, combined with $Zn_2SiO_4(001)$, and the interface spacing was set to 2.2A.

Atoms within a range of 3.5 Å above and below the center of the interface were selected as the heterogeneous interface. The MSD of Zn^{2+}, Al^{3+}, and Si^{4+} was calculated, and by analyzing the time-dependent behavior of the MSD at different temperatures, the migration behavior of cations near the interface and its temperature dependence were investigated.

In order to further study the effect of temperature on the ability of ions to migrate in the direction perpendicular to the interface, the MSD in the z-axis direction was calculated between 1000 K and 1500 K with an interval of 50 K. The obtained slope values are summarized in Fig. 7. For Zn^{2+}, Al^{3+} and Si^{4+}, the MSD in the z-axis direction usually increases with increasing temperature. At the same temperature, Zn^{2+} has the largest MSD in the z-axis direction, followed by Si^{4+}, and Al^{3+} has the smallest slope.

Therefore, within the studied temperature range and under the current interface model, the order of migration abilities of these three cations perpendicular to the interface direction is Zn^{2+} > Si^{4+} > Al^{3+}. Reflects the growth rate of displacement of ions perpendicular to the interface, and also indicates their different trends across the interface.

The Z-direction MSD slope of Zn^{2+} increases significantly between 1400–1450 K, indicating that its atomic displacement along the interface normal direction is significantly enhanced. To further study this phenomenon, the cross-interface migration behavior at different temperatures was statistically calculated. The results show that compared with 1400 K, the cross-interface migration behavior of Zn is significantly enhanced at 1450 K, and the average penetration depth increases, indicating that Zn atoms can migrate farther to the other side of the interface at higher temperatures. Fig. 8 shows the MSD of Zn^{2+} at 1400K and 1450K.

In order to explore the stability of the interface structure and the local coordination characteristics of cations in high-temperature environments, the total radial distribution function (RDF), partial radial distribution function and coordination number of the system at 1500 K were calculated. It can be seen from the total RDF in Fig. 9 that the system has an obvious first main peak at about 1.9 Å. There are strong short-range correlations between atoms. As the atomic distance increases, the RDF curve exhibits multiple broadened secondary peaks. The system still retains certain mid-range structural correlations, but at the same time there is structural disorder caused by high-temperature thermal perturbations. This feature of the total RDF indicates that despite the high temperature promoting atomic motion, the system retains distinct local structural features.

To reveal the Zn-O coordination environment, statistical analysis of all frame molecular dynamics trajectories was performed. As shown in Fig. 10, four-coordinated Zn accounts for the highest proportion, reaching 50.448%; three-coordinated and five-coordinated Zn account for 20.541% and 22.923% respectively, and six-coordinated and higher-coordinated environments only account for about 4.804%. The average Zn-O coordination number is 4.096 and the standard deviation is 0.823. The above results indicate that although four-coordination is still the main local coordination form of Zn, the Zn-O coordination environment at high temperatures is not completely fixed, but exhibits obvious local structural heterogeneity. The coexistence of three-coordination and five-coordination structures may be related to the local rearrangement of oxygen atoms and the dynamic adjustment of the Zn-O coordination shell caused by thermal perturbation.

As shown in Fig. 11, at 1500K, the 15-70 ps interval was selected to analyze the MSD logarithmic curve in the z direction. At the same time, a hopping threshold of 2.8Å and a dwell time of 2.0ps were used to count cation hopping events. The cation jump distance distributions of Zn^{2+}, Si^{4+}, and Al^{3+} are shown in Fig. 12.The power index of Zn^{2+} is 0.92, which is close to 1. Its diffusion behavior along the interface-normal direction is approximately Fickian. The power index of Si^{4+} is 0.81, showing weakly

subdiffusive behavior in the z direction. The power index of Al^{3+} is 1.18. This slightly larger than 1. This is caused by its low transition frequency and insufficient statistical samples.

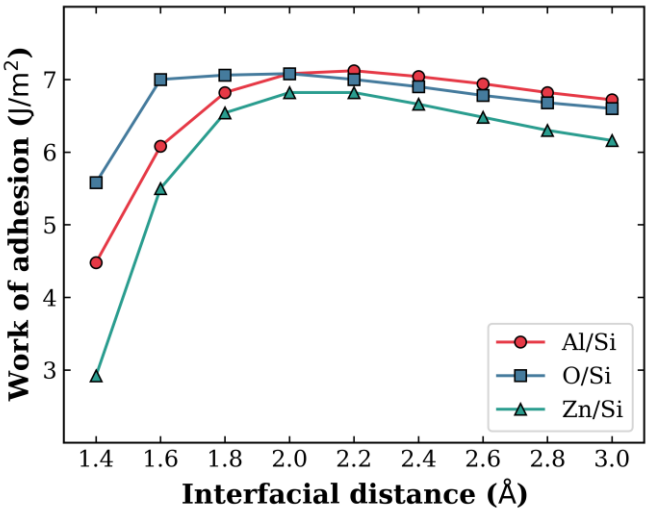

Fig. 6. Curve chart of adhesion work of three heterogeneous interface models as a function of interfacial spacing

Table 2

Optimal interface spacing and adhesion work of three heterogeneous interface models

Stacking method	Optimal interface spacing(Å)	$W_{ad}(J/m^2)$
-Al-Si-	2.2	7.12
-Zn-Si-	2.0	6.82
-O-Si-	2.0	7.08

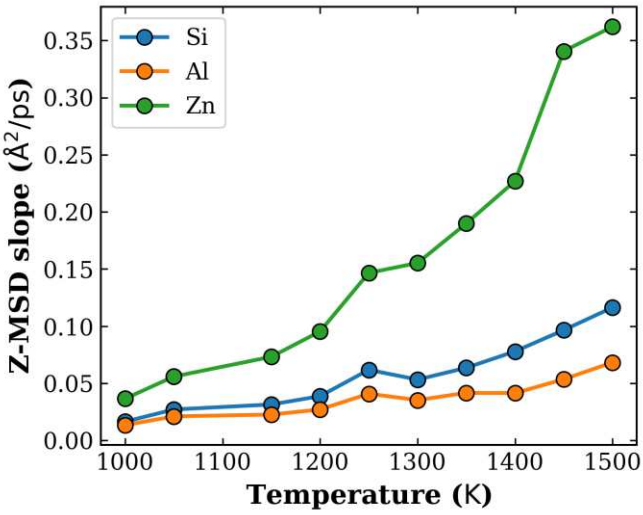

Fig. 7. Z-direction MSD of cations in the 1000-1500 K range

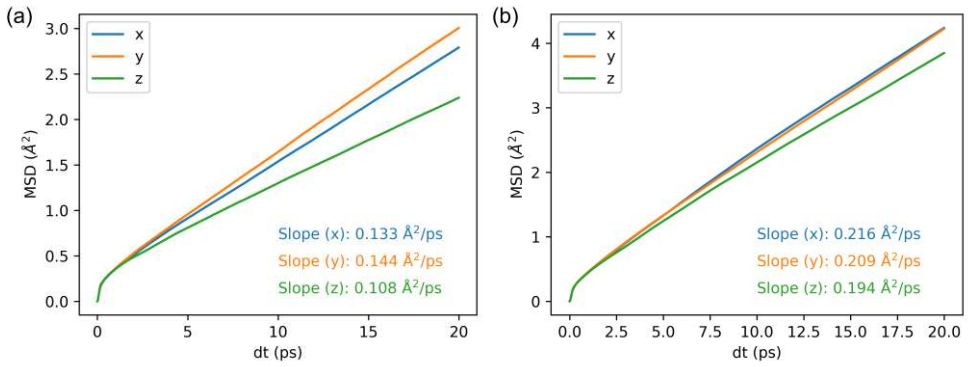

Fig. 8. MSD of Zn^{2+} (a)1400K and (b)1450 K

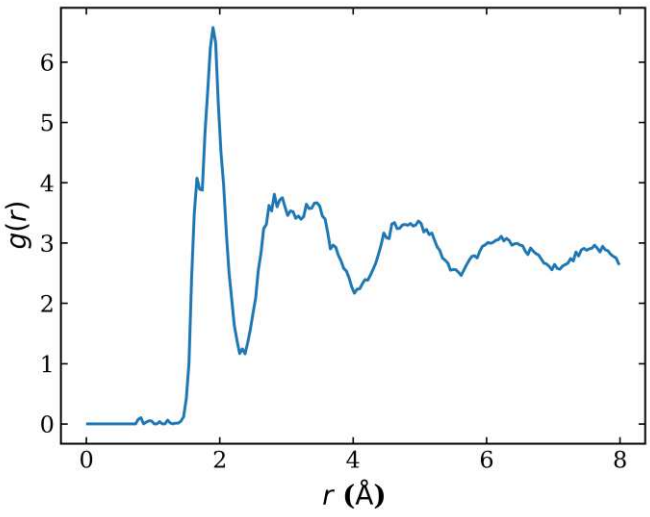

Fig. 9. Radial distribution function for heterogeneous interface

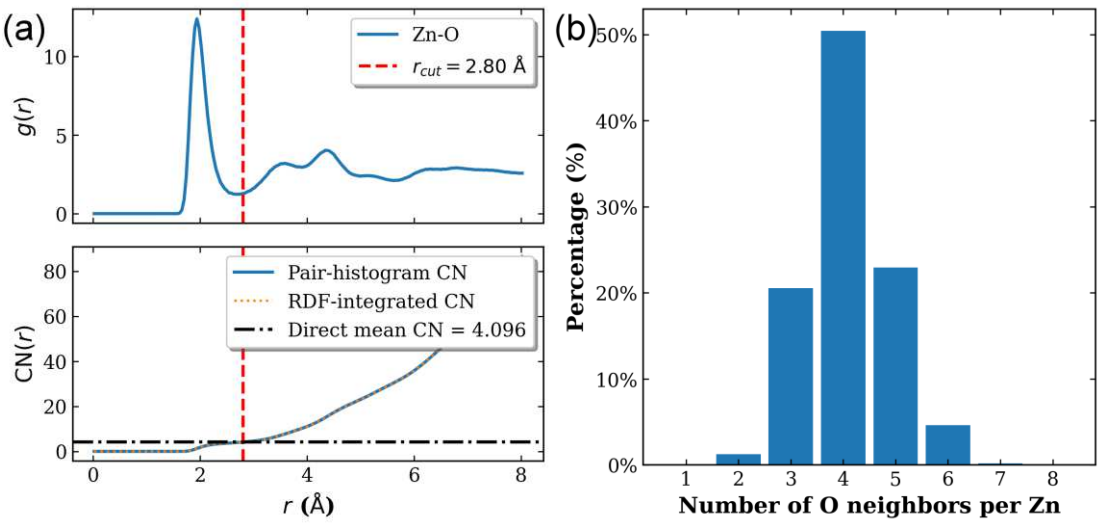

Fig. 10. Radial distribution function and coordination number for Zn^{2+}

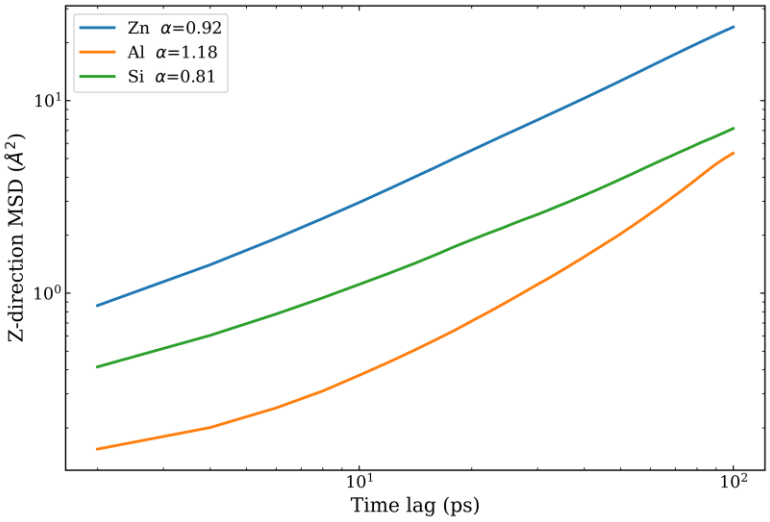

Fig. 11. Log-log plot of the z-direction MSD for Zn^{2+}, Al^{3+} and Si^{4+}

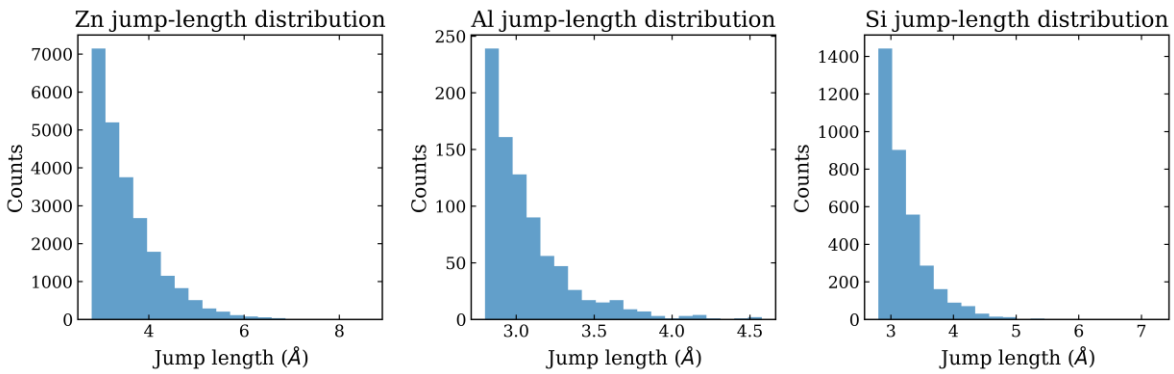

Fig. 12. Jump length distributions of Zn^{2+}, Al^{3+} and Si^{4+}

4. Conclusions and Outlook

This study combines DFT, NEP and MLMD methods to study the cation diffusion mechanism in $ZnAl_2O_4$, Zn_2SiO_4 and $ZnAl_2O_4/Zn_2SiO_4$ heterogeneous interface systems. The main conclusions are as follows.

In the bulk lattice, the diffusion of all doped cations can be approximated by the Arrhenius form in a limited temperature range. This study calculated the diffusion activation energy of the self-diffusion of doped cations and obtained their respective diffusion Arrhenius expressions. In $ZnAl_2O_4$, the diffusion coefficient roughly follows the order $B^{3+} > Ti^{4+} > Si^{4+}$, while in Zn_2SiO_4 the order of diffusion coefficient is $B^{3+} > Al^{3+} > Ti^{4+}$. These results indicate that cation diffusion is affected by the combined influence of diffusion activation energy, pre-exponential factors, and local atomic environment, rather than by ion size or activation energy alone.

Interfacial adhesion force calculations show that the $ZnAl_2O_4(111)/Zn_2SiO_4(001)$ interface with Al atom cutoff exhibits the highest calculated adhesion work among the three interface structures studied. Therefore, this structure with an optimized interfacial spacing of 2.2 Å was selected for subsequent MLMD simulations.

At the $ZnAl_2O_4/Zn_2SiO_4$ heterointerface, the Z-direction MSD slopes of Zn^{2+}, Si^{4+} and Al^{3+} generally increase with increasing temperature. Under the studied conditions, the migration-related displacements along the interface normal direction follow the order $Zn^{2+} > Si^{4+} > Al^{3+}$. In particular, Zn^{2+} shows a significant enhancement of interfacial migration behavior between 1400 and 1450 K. This temperature-related enhancement is further supported by cross-interface migration statistics, showing increased migration activity and penetration depth at higher temperatures. These findings highlight the different temperature responses of different cations near heterogeneous interfaces.

This study analyzed the temperature dependence of cation diffusion in bulk doped systems. The atomic motion characteristics in the vicinity of the $ZnAl_2O_4/Zn_2SiO_4$ heterointerface were explored. Limited by the simulation time of 200 ps, it is difficult to fully characterize the long-term diffusion and interface reactions in the actual sintering process in this work. The obtained results reveal the cation migration and its temperature dependence from the atomic scale. This provides theoretical support for understanding the temperature response of interface atoms, elucidating the interface diffusion mechanism and optimizing the co-firing process of ceramic-ferrite composites.

Acknowledgements

This work is financially supported by the National Natural Science Foundation of China (project U2341263).

Author contributions

All authors participated in the conception and design of this study. Kaixin Zhang was responsible for the conceptualization, survey research, method design, data collection and formal analysis of this study, and completed the writing of the first draft and the

review and revision of the manuscript. Peng Bi and Yong Yi participated in method design and software development, and were responsible for supervision, guidance and verification. Jingsong Liu, Enzhu Li and Xu Huang were responsible for funding acquisition, project management, supervision, guidance and verification, and manuscript review and revision. Each author provided revisions to several versions of the first draft, and the final draft was reviewed and approved by all authors.

Data availability

Data will be made available on request.

Declaration

Conflict of interest

The authors declare that they have no known competing financial interests or personal relationships that could have appeared to influence the work reported in this paper.

References

[1] W. Luo, S. Yan, J. Zhou, Ceramic-based dielectric metamaterials, Interdisciplinary Materials 1 (2022) (1) 11-27.

[2] X. Bai, Y. Yin, J. Zhang, Miniature high performance LTCC bandpass filter with multiple controllable transmission zeros, 2023 IEEE 11th Asia-Pacific Conference on Antennas and Propagation (APCAP) (2023), p.1-2.

[3] N. Javanbakht, R.E. Amaya, J. Shaker, B. Syrett, A Compact Cavity-Based Leaky-Wave Antenna in a Low Temperature Co-Fired Ceramic Process With Improved Performance, IEEE Access 9 (2021) 25014-25024.

[4] K.-S. Chin, W. Jiang, W. Che, C.-C. Chang, H. Jin, Wideband LTCC 60-GHz Antenna Array With a Dual-Resonant Slot and Patch Structure, IEEE Transactions on Antennas and Propagation 62 (2014) (1) 174-182.

[5] B. You, H.-Y. Li, J.-X. Xu, X.Y. Zhang, Design of Low-Loss High-Selectivity LTCC Bandpass Filter, 2025 International Conference on Microwave and Millimeter Wave Technology (ICMMT) (2025), p.1-3.

[6] W. Tang, R. Xu, L. Zhao, A Miniaturized Bandpass Filter Based on LTCC, 2023 International Conference on Microwave and Millimeter Wave Technology (ICMMT) (2023), p.1-3.

[7] M. Matters-Kammerer, U. Mackens, K. Reimann, R. Pietig, D. Hennings, B. Schreinemacher, R. Mauczok, S. Gruhlke, C. Martiny, Material properties and RF applications of high k and ferrite LTCC ceramics, Microelectronics Reliability 46 (2006) (1) 134-143.

[8] M. Heidenreich, J. Schur, J. Mueller, W. Gitzel, A.F. Jacob, J. Töpfer, Hexagonal ferrites for self-biasing circulators integrated in LTCC microwave modules, Materials Research Bulletin 178 (2024) 8.

[9] Y.-H. Kim, D.-K. Park, K.-H. Koo, Design of Multiple-Receiving WPT System Using Ferrite-Embedded LTCC, IEICE Transactions on Communications E103.B (2020) (3) 247-252.
[10] S.V. Sidorova, S.A. Khokhlun, The Properties Investigation Results of Low-Temperature Co-Fired Ceramics, 2025 7th International Youth Conference on Radio Electronics, Electrical and Power Engineering (REEPE) (2025), p.1-6.
[11] O.Y. Hong, S.-H. Min, Factors Influencing the Camber of Cofired Resistor/Low Temperature Cofired Ceramics (LTCC) Bi-Layers, Korean Journal of Materials Research 33 (2023) (12) 537-549.
[12] H.Y. Zhang, Z. Yu, X.N. Jiang, X.F. Zhang, Q.F. Su, J. Zhuo, C.J. Wu, Q.F. Li, K. Sun, Z.W. Lan, Phenomenon and mechanism of ion diffusion at Co-fired joint interface of NiZn Ferrite/MCT ceramic heterostructure, Ceramics International 49 (2023) (12) 20682-20687.
[13] Z.X. Li, H.C. Yang, H.Y. Yang, E.Z. Li, Probing interfacial ionic diffusion and stress in LTCC-LTCF heterostructures: mechanisms and implications for co-fired compatibility, Applied Surface Science 720 (2026) 9.
[14] X.M. Zhang, C. Qu, Y.Y. Li, Y.T. Kang, L.Y. Pu, X. Huang, J.S. Liu, Microstructure, sinterability and properties of ZnO-B2O3-SiO2 glass/ Al2O3 composites for LTCC application, J. Mater. Sci.-Mater. Electron. 36 (2025) (24) 12.
[15] G. Jáger, J.J. Tomán, L. Juhász, Z. Erdélyi, C. Cserháti, G. Vecsei, Nucleation and growth kinetics of ZnAl2O4 spinel in crystalline ZnO - amorphous Al2O3 bilayers prepared by atomic layer deposition, Scr. Mater. 219 (2022) 5.
[16] H. Dixit, N. Tandon, S. Cottenier, R. Saniz, D. Lamoen, B. Partoens, First-principles study of possible shallow donors in ZnAl2O4 spinel, Phys. Rev. B 87 (2013) (17) 7.
[17] C.L. Muhich, V.J. Aston, R.M. Trottier, A.W. Weimer, C.B. Musgrave, First-Principles Analysis of Cation Diffusion in Mixed Metal Ferrite Spinels, Chemistry of Materials 28 (2016) (1) 214-226.
[18] O.T. Unke, S. Chmiela, H.E. Sauceda, M. Gastegger, I. Poltavsky, K.T. Schütt, A. Tkatchenko, K.-R. Müller, Machine Learning Force Fields, Chemical Reviews 121 (2021) (16) 10142-10186.
[19] P.-L. Kang, C. Shang, Z.-P. Liu, Large-Scale Atomic Simulation via Machine Learning Potentials Constructed by Global Potential Energy Surface Exploration, Accounts of Chemical Research 53 (2020) (10) 2119-2129.
[20] S.K. Achar, J. Schneider, D.A. Stewart, Using Machine Learning Potentials to Explore Interdiffusion at Metal–Chalcogenide Interfaces, ACS Applied Materials & Interfaces 14 (2022) (51) 56963-56974.
[21] M. Tahani, E. Postek, T. Sadowski, Diffusion and Interdiffusion Study at Al- and O-Terminated Al2O3/AlSi12 Interface Using Molecular Dynamics Simulations, Materials 16 (2023) (12).
[22] K. Noordhoek, C.J. Bartel, Accelerating the prediction of inorganic surfaces with machine learning interatomic potentials, Nanoscale 16 (2024) (13) 6365-6382.
[23] J. Dai, Y. Jiang, W. Lai, Study of diffusion and conduction in lithium garnet oxides

LixLa3Zrx-5Ta7-xO12 by machine learning interatomic potentials, Physical Chemistry Chemical Physics 24 (2022) (24) 15025-15033.
[24] S.H. Yu, P. Bi, J.S. Liu, E.Z. Li, Y. Yi, Machine learning molecular dynamics investigation on cation diffusion mechanisms in Ni0.2Cu0.3Zn0.5Fe2O4 ferrite and its homogeneous interfaces, Solid State Ion. 439 (2026) 9.
[25] C.B. Chen, Y.T. Li, R. Zhao, Z.L. Liu, Z.Y. Fan, G. Tang, Z.Y. Wang, NepTrain and NepTrainKit: Automated active learning and visualization toolkit for neuroevolution potentials, Comput. Phys. Commun. 317 (2025) 11.
[26] G. Kresse, J. Furthmüller, Efficient iterative schemes for ab initio total-energy calculations using a plane-wave basis set, Phys. Rev. B 54 (1996) (16) 11169-11186.
[27] G. Kresse, D. Joubert, From ultrasoft pseudopotentials to the projector augmented-wave method, Phys. Rev. B 59 (1999) (3) 1758-1775.
[28] E. German, R. Faccio, A.W. Mombrú, A DFT + U study on structural, electronic, vibrational and thermodynamic properties of TiO2 polymorphs and hydrogen titanate: tuning the Hubbard 'U-term', Journal of Physics Communications 1 (2017) (5) 055006.
[29] Z.Y. Fan, Z.Z. Zeng, C.Z. Zhang, Y.Z. Wang, K.K. Song, H.K. Dong, Y. Chen, T.A. Nissila, Neuroevolution machine learning potentials: Combining high accuracy and low cost in atomistic simulations and application to heat transport, Phys. Rev. B 104 (2021) (10) 15.
[30] H. Eslami, F. Mojahedi, J. Moghadasi, Molecular dynamics simulation with weak coupling to heat and material baths, J. Chem. Phys. 133 (2010) (8) 7.
[31] C. Kirse, M. Kindlein, F. Luxenburger, E. Elts, H. Briesen, Analysis of two common algorithms to compute self-diffusion coefficients in infinite dilution from molecular dynamics simulations and application to n-alkanes (C1 to C35) in water, Fluid Phase Equilib. 485 (2019) 211-219.
[32] N. Srinatha, K.J. Rudresh Kumar, M.R. Suresh Kumar, A. Madhu, B. Angadi, A novel combustion fuel for the synthesis of nanocrystalline ZnAl2O4 particles based on the thermodynamic correlations and their structural and optical studies, Ceramics International 48 (2022) (3) 3669-3675.
[33] X. Mei, J. Hao, Q. Liu, Z. Zhu, S. Bai, F. Wang, Fabrication and characterization of porous ZnAl2O4 ceramics, Ceramics International 51 (2025) (22) 37220-37229.
[34] S. Mathur, M. Veith, M. Haas, H. Shen, N. Lecerf, V. Huch, S. Hüfner, R. Haberkorn, H.P. Beck, M. Jilavi, Single-Source Sol-Gel Synthesis of Nanocrystalline ZnAl2O4: Structural and Optical Properties, Journal of the American Ceramic Society 84 (2004) (9) 1921-1928.
[35] E. Huízar-Padilla, H. Guillén-Bonilla, A. Guillén-Bonilla, V.-M. Rodríguez-Betancourtt, A. Sánchez-Martínez, J.T. Guillen-Bonilla, L. Gildo-Ortiz, J. Reyes-Gómez, Synthesis of ZnAl2O4 and Evaluation of the Response in Propane Atmospheres of Pellets and Thick Films Manufactured with Powders of the Oxide, Sensors 21 (2021) (7).
[36] X. Yuan, X. Tan, B. Liu, Structural, Mechanical, Electronic and Optical Properties of Spinel ZnAl2O4 Underpressure from First-Principles Calculations, Russian

Journal of Physical Chemistry B 17 (2023) (4) 886-895.
[37] S. Mandal, J.G. Hemrick, M.K. Mahapatra, Zinc aluminate (ZnAl2O4) refractory aggregates: Dilatometric sintering studies and thermal expansion coefficient, Journal of the European Ceramic Society 42 (2022) (13) 6244-6254.
[38] R.F. Samigullina, A.P. Tyutyunnik, I.N. Gracheva, T.I. Krasnenko, N.A. Zaitseva, T.A. Onufrieva, Hydrothermal synthesis of α-Zn 2 SiO 4 :V phosphor, determination of oxidation states and structural localization of vanadium ions, Materials Research Bulletin 87 (2017) 27-33.
[39] M.H.M. Zaid, K.A. Matori, Y. Yaakob, I.M. Alibe, Simple thermal treatment approach for the synthesis of α-Zn2SiO4 nanoparticles, Optics & Laser Technology 140 (2021).
[40] J. Yang, H. Li, R. Liu, X. Xiong, J. Chen, Enhanced microstructure and dielectric properties of Zn2SiO4-based ceramics via microwave sintering, Journal of Materials Science: Materials in Electronics 36 (2025) (21).
[41] S.Z. Karazhanov, P. Ravindran, P. Vajeeston, A.G. Ulyashin, H. Fjellvåg, B.G. Svensson, Phase stability and pressure-induced structural transitions at zero temperature in ZnSiO3and Zn2SiO4, Journal of Physics: Condensed Matter 21 (2009) (48).
[42] R. Dai, R. Cheng, J. Wang, C. Zhang, C. Li, H. Wang, X. Wang, Y. Zhou, Tunnel-structured willemite Zn2SiO4: Electronic structure, elastic, and thermal properties, Journal of Advanced Ceramics 11 (2022) (8) 1249-1262.